J. Indian Inst. Sci.
A Multidisciplinary Reviews Journal
ISSN: 0970-4140 Coden-JIISAD

Interference in Quantum Mechanics

Urbasi Sinha[1,2*] *and Debadrita Ghosh*[1]

Abstract | Physicist and Nobel Laureate Richard P. Feynman once remarked, "We choose to examine a phenomenon which is impossible, *absolutely* impossible, to explain in any classical way, and which has in it the heart of quantum mechanics. In reality, it contains the only mystery. We cannot make the mystery go away by "explaining" how it works. We will just tell you how it works. In telling you how it works, we will have told you about the basic peculiarities of all quantum mechanics"[1]. The phenomenon of interference is ubiquitous in the quantum world and indeed holds within itself the explanation for many counterintuitive quantum phenomena. In this review, we choose to focus on a few ramifications and manifestations of quantum interference that have deep implications for the foundations of quantum mechanics. These include single-photon or second-order interference, two-photon or fourth-order interference and higher-order interference.

1 One-Photon Interference

1.1 Single-Photon-Sources

Before exploring quantum interference with photons, it is important to understand what a single photon is. A photon is the smallest unit of light, representing an elementary excitation of a single mode of the quantized electromagnetic field. Each mode, labeled by its frequency (ν_k), corresponds to photons with energy ($h\nu_k$), where h is Planck's constant. A single photon in the ideal state is represented as $|1\rangle_k$, where k defines the mode of the field. This mode may describe the photon's spatial distribution, spectral characteristics, or temporal structure.

Photons interact weakly with their environment and can travel long distances at the speed of light, resulting in minimal noise and loss. They can also be easily manipulated using linear optics. These properties make photons an excellent platform for encoding information as photonic qubits, where the quantum state of the photon–such as its polarization, momentum, or energy–serves as the carrier of information. As a result, single photons are essential for applications in quantum computation and quantum information science, enabling secure communication, precise manipulation, and efficient data processing.

An ideal single-photon source produces one photon at a time in a specific mode, ensuring that the photon's properties remain consistent with every emission. In practice, a perfect single-photon source cannot be achieved due to losses and the presence of multiphoton emissions. In terms of statistics, Poissonian and super-Poissonian distributions can be explained by classical wave theory, whereas sub-Poissonian statistics cannot. The observation of sub-Poissonian statistics provides strong evidence for the quantized nature of light.

There are various physical methods to generate single photons. Single-photon sources can be broadly classified into two categories: deterministic and probabilistic. Deterministic sources rely on systems such as colour centres, quantum dots, and single atoms, producing photons at fixed intervals. Probabilistic single-photon sources often utilize phenomena like Spontaneous Parametric Down-Conversion (SPDC) in nonlinear crystals, where photon pairs are generated by a pump laser. A key advantage of this method is that one photon (called the idler or heralding photon) signals the creation of the other photon

[1] Raman Research Institute, Sadashivanagar, 560080 Bengaluru, India.
[2] Department of Physics and Astronomy, Calgary T2N 1N4, Alberta, Canada.
*usinha@rri.res.in

Springer IISc PRESS

(called the signal or heralded photon). In principle, the exact timing of the signal cannot be predicted. However, by using a pulsed pump laser, the heralding signal can be predicted within the pulse width time. For a more detailed discussion on different types of single-photon sources and their properties, readers are encouraged to consult the references[2,3].

1.2 Interference in Quantum Mechanics

Quantum interference is rooted in the concept of the superposition of probability amplitudes from processes contributing to a given phenomenon. As Dirac famously stated, "Each photon interferes only with itself." He explained that in quantum mechanics, the entities that interfere are not particles but probability amplitudes for specific events. It is the fact that these probability amplitudes add like complex numbers that give rise to all quantum mechanical interferences[4].

In classical mechanics, superposition produces a distinct and definite new state. In contrast, in quantum mechanics, superposition does not result in a definite new state but instead alters the probabilities of the system being observed in its basis states. In classical mechanics, interference is described through the division of amplitude, which inherently leads to a division of energy. In quantum mechanics, however, interference is described through the division of the wave function, which does not imply a division of energy, as a photon cannot be divided. In the case of a Mach-Zehnder interferometer, two physical waves with independent energies can be mutually coherent, allowing them to interfere. In the quantum picture, however, each individual photon simultaneously exists in both arms of the interferometer, with finite probability amplitudes that interfere with one another.

In classical wave theory, when two coherent waves interfere, their amplitudes add up algebraically. The waves may come from two different sources, such as two slits in a double-slit experiment or two arms in a Mach-Zehnder interferometer. Let's consider two waves travelling in the same direction. The electric fields of these waves at a given point are E_1, and E_2, and we assume they are coherent. The total electric field E_{total} is the sum of the individual electric fields. For simplicity, let's assume the two waves have the same amplitude A, so: $E_1 = A\cos(\omega t + \phi_1)$, and $E_2 = A\cos(\omega t + \phi_2)$. The total electric field will be: $E_{total} = A\cos(\omega t + \phi_1) + A\cos(\omega t + \phi_2)$ $= 2A\cos(\frac{\phi_1+\phi_2}{2})\cos(\frac{\phi_1-\phi_2}{2})$. The intensity is proportional to the square of the total amplitude:

$$I_{total} \propto |E_{total}|^2 = 4A^2\cos^2(\frac{\phi_1+\phi_2}{2})\cos^2(\frac{\phi_1-\phi_2}{2}) \quad (1)$$

$\cos(\frac{\phi_1+\phi_2}{2})$ describes a modulation factor that accounts for the combined effect of both phases. The factor $\cos^2(\frac{\phi_1-\phi_2}{2})$ reflects how the interference varies as a function of the phase difference, $(\phi_1 - \phi_2)$ and this causes the intensity to oscillate between constructive interference and destructive interference. The amplitude of the resulting wave is directly related to the sum of the amplitudes of the individual waves. The electric fields E_1 and E_2 are added (or subtracted), meaning they divide the total amplitude into contributions from each wave.

In quantum mechanics, a system is described by a wave function ψ. The wave function $\psi(x)$ at a position x gives the probability amplitude for the photon to be found at that location. The probability of detecting the photon at x is proportional to the square of the magnitude of the wave function: $P(x) = |\psi(x)|^2$. This gives us a probability distribution, which tells us where the photon is most likely to be detected, but it is not a deterministic prediction. The photon does not "choose" a single path or location until it is observed; rather, it exists in a superposition of all possible paths. In a Mach-Zehnder interferometer, the photon takes both paths simultaneously, and the two paths are described by separate probability amplitudes, ψ_1, and ψ_2. The total wave function at the detector is the sum of these probability amplitudes: $\psi_{total} = \psi_1 + \psi_2$. The probability of detecting the photon is related to the square of the total wave function:

$$P_{det} = |\psi_{total}|^2 = |\psi_1|^2 + |\psi_2|^2 + 2\mathcal{R}(\psi_1^*\psi_2) \quad (2)$$

The photon's energy is not divided between the two arms of the interferometer; instead, the probabilities for detecting the photon are modified due to the interference between the probability amplitudes.

1.3 Interferometer Components

In photonic architectures, an interferometer typically consists of passive linear optical components, such as Beam-Splitters (BS), mirrors, and waveplates. It has input ports where light enters and output ports that record either photon counts in the single-photon regime or photocurrent proportional to the laser intensity.

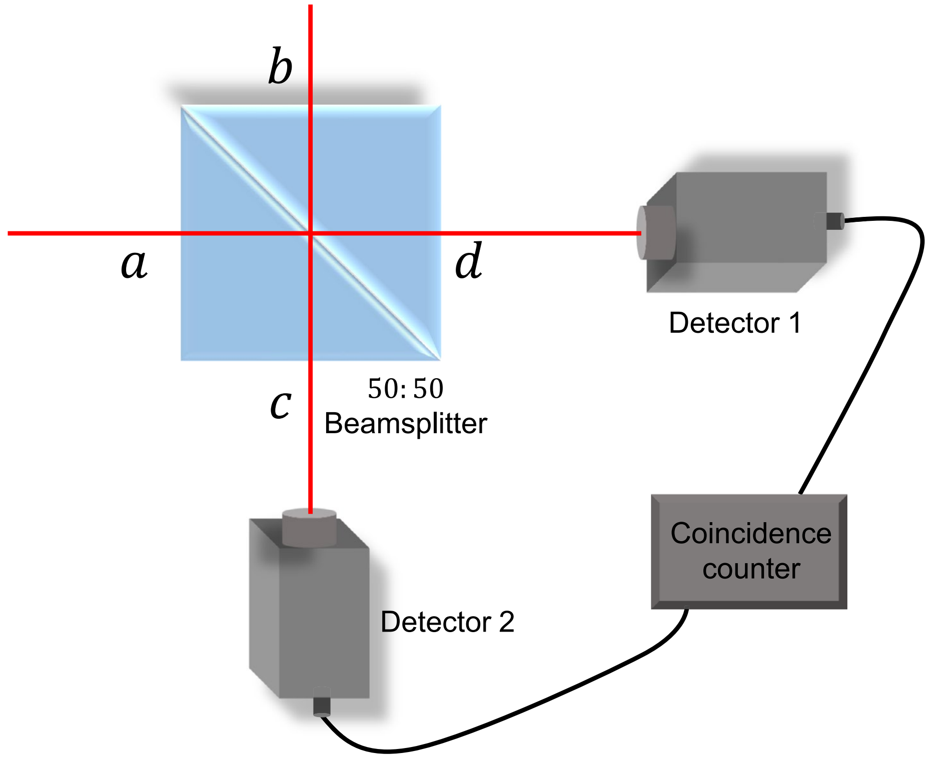

Figure 1 The schematic illustrates the HBT interference setup. A 50 : 50 BS is shown with two input ports (**a** and **b**) and two output ports (**c** and **d**). Detectors are positioned at the **c** and **d** output ports to measure the intensities. The correlation between the measured intensities is determined using a coincidence counter.

A BS is a key component in many practical interferometers. It splits incident light into two separate beams–one transmitted and the other reflected–at a specific ratio. A BS has two input ports and two output ports. Light entering through one input port is split, with the transmitted and reflected components measured at the two output ports. Alternatively, light can enter through both input ports simultaneously, and the resulting split beams can be observed at both output ports. While a BS is a straightforward device from the perspective of classical physics, its behaviour becomes complex and non-trivial in the context of quantum mechanics. The statistical behaviour of photons at the BS output changes, giving rise to fundamental quantum phenomena such as quantum superposition and randomness. A BS can also create entanglement between the output fields[5,6].

In the quantum mechanical description, the input and output fields of a BS are represented by operators. As shown in Fig. 1, the input ports of the BS are labeled a and b, while the output ports are labeled c and d. A mathematical relationship connects the input and output operators. The input modes a and b are associated with the annihilation and creation operators $\hat{a}$, $\hat{a}^\dagger$ and $\hat{b}$, $\hat{b}^\dagger$, respectively. Similarly, the output modes c and d correspond to the annihilation and creation operators $\hat{c}$, $\hat{c}^\dagger$ and $\hat{d}$, $\hat{d}^\dagger$, respectively. The input–output transformation matrix can be expressed by replacing the classical electric field components with their corresponding quantum operators.

$$\begin{pmatrix} \hat{c} \\ \hat{d} \end{pmatrix} = \begin{pmatrix} R & T \\ T & R \end{pmatrix} \begin{pmatrix} \hat{a} \\ \hat{b} \end{pmatrix} \tag{3}$$

Here, T and R represent the transmission and reflection coefficients of a BS, respectively. Both T and R are complex numbers. For a lossless BS, the BS matrix is unitary, meaning $|T|^2 + |R|^2 = 1$, and also $R^*T + T^*R = 0$. Starting from the Eq. 3, it can also be expressed as,

$$\begin{pmatrix} \hat{a} \\ \hat{b} \end{pmatrix} = \begin{pmatrix} R^* & T^* \\ T^* & R^* \end{pmatrix} \begin{pmatrix} \hat{c} \\ \hat{d} \end{pmatrix} \tag{4}$$

In the case of a 50 : 50 BS, the transmission and reflection coefficients each correspond to 50% of the incident light, giving a complex amplitude of $\frac{1}{\sqrt{2}}$. If the BS is symmetric, the reflection introduces a phase shift of $\frac{\pi}{2}$ relative to the transmission. So, the BS matrix is expressed as $\frac{1}{\sqrt{2}}\begin{pmatrix}1 & i\\ i & 1\end{pmatrix}$.

A basic interferometer can be created using a BS, which demonstrates the Hanbury Brown-Twiss (HBT) effect. Although the setup is simple, the HBT interference effect remains a landmark experiment in quantum optics[7].

1.4 Theoretical Derivation of HBT Interference

In this effect, light passes through a BS and reaches two detectors at the two output ports. The correlation of the intensities measured by these detectors is recorded. The key observation of the HBT effect is that the correlation between the light intensity at two different detectors can reveal the properties of the light. The second-order correlation function $g^{(2)}(\tau)$ quantifies the correlation between the intensities measured at the two detectors at different times. If l_1 is the optical path length traversed by light from the BS to the detector at output port c, and l_2 is the optical path length traversed by light from the BS to the detector at output port d, then the time delay τ is given by $\tau = \frac{|l_1 - l_2|}{c}$, where c is the speed of light. If light with intensity I is incident on a BS, $I_c(t)$ and $I_d(t+\tau)$ represent the intensities measured by the detectors at output ports c and d at times t and $(t+\tau)$, respectively. The normalized correlation function of the light intensity is then given by:

$$g^{(2)}(\tau) = \frac{\langle I_c(t) I_d(t+\tau)\rangle}{\langle I_c(t)\rangle \langle I_d(t+\tau)\rangle} \tag{5}$$

$g^{(2)}$ measures how correlated the intensities at the two detectors are. For a $50:50$ beam splitter, when $\tau = 0$, the $g^{(2)}$ equals 1 for classical light.

In quantum mechanics, photons are described using the Fock state formalism. When a single photon is incident on the BS, its state is $|1\rangle_a|0\rangle_b$. A single photon in a specific mode is represented by applying the creation operator to the vacuum state of that mode, expressed as $|1\rangle_a|0\rangle_b = \hat{a}^\dagger|0\rangle_a|0\rangle_b$. From Eq. 4, $\hat{a}^\dagger = R\hat{c}^\dagger + T\hat{d}^\dagger$. Therefore, the output state is,

$$|\psi_{HBT}\rangle = (R\hat{c}^\dagger + T\hat{d}^\dagger)\,|0\rangle_c|0\rangle_d = R\,|1\rangle_c|0\rangle_d + T\,|0\rangle_c|1\rangle_d \tag{6}$$

This represents the superposition state of a photon being in output port c or a photon being in port d. For a $50:50$ BS, the output state is,

$$|\psi_{HBT}\rangle = \frac{1}{\sqrt{2}}(i|1\rangle_c|0\rangle_d + |0\rangle_c|1\rangle_d) \tag{7}$$

The average number of photons in port c is given by the expectation value of the number operator $\hat{a}^\dagger\hat{a}$, which evaluates to $\langle\psi_{HBT}|\hat{a}^\dagger\hat{a}|\psi_{HBT}\rangle = |R|^2 = \frac{1}{2}$. The same result holds for output port d.

If we repeat the measurement many times, half of the incident photons are detected by the detector in port c, and the other half are detected by the detector in port d. This result aligns perfectly with classical predictions. However, when examining the correlation between the detected photons in both output ports, non-classicality becomes evident. In calculating $g^{(2)}$ using Eq. 5 the average intensity $\langle I_c(t) I_d(t+\tau)\rangle$ is replaced by photon number operator. The expectation value of the photon number operator then gives the photon count in practice. At $\tau = 0$, the expression for $g^{(2)}$ is then given by,

$$g^{(2)}(\tau = 0) = \frac{\langle \hat{c}^\dagger\, \hat{c}\, \hat{d}^\dagger\, \hat{d}\rangle}{\langle \hat{c}^\dagger\, \hat{c}\rangle\, \langle \hat{d}^\dagger\, \hat{d}\rangle} \tag{8}$$

This result yields a value of 0, which is a hallmark of quantum behaviour. This outcome serves as a crucial test for the single-photon source, confirming that it indeed generates photons one at a time.

2 Two-Photon interference

The interference of two photons generated simultaneously through parametric down-conversion was analyzed in 1986[8]. The study explored fourth-order interference effects, distinct from standard second-order interference involving single-field quantities. These effects were observed by measuring the joint probability of detecting both photons at two points in the interference plane using photoelectric detectors. The joint detection probability exhibited cosine-like modulation with visibility approaching 100% under ideal conditions. In 1987, C.K. Hong, Z.Y. Ou, and L. Mandel conducted a seminal experiment demonstrating a quantum interference effect when indistinguishable photons were incident on a $50:50$ BS[9]. This phenomenon, known as "photon bunching," resulted in the two photons exiting the BS together in the same output port. The authors have demonstrated the measurement of extremely short time intervals between two photons, providing insights into the length of the photon wave packet. This was further investigated by[10], where the researchers demonstrated that, unlike second-order interference, which is absent due to the lack of a definite phase relationship between photons, fourth-order interference manifested through joint probability measurements of photon detection at two positions. The interference exhibited 100% visibility, revealing nonclassical features. These results aligned with quantum predictions and contrasted with classical wave theories, which predicted a maximum visibility of only 50%. The theory of fourth-order interference using a BS has been explored in detail[11], including the conditions under which classical and quantum fields exhibit interference. In 1988, Y.H. Shih, and C.O. Alley conducted an experiment[12] with correlated photons generated from a nonlinear crystal via down conversion. They measured both coincidence counts and single counts and then calculated the ratio between them. Polarizers were placed in front of the detectors to create different polarization eigenstates. The results showed that the ratio reached its maximum when the polarization axes were perpendicular and its minimum when the axes were parallel.

Around the same period, Fearn and Loudon explored theoretical frameworks of two-photon interference[13] for different types of photon sources. The authors calculated the second factorial moments of photocounts and the cross-correlation function for the two output arms of a lossless BS. When photon pairs enter the BS through separate input arms and arrive simultaneously, the output state where one photon is detected in each arm is strongly suppressed. This suppression is evident in the photo count cross-correlation, which can vanish for certain input parameters from two-atom or parametric oscillator sources and is reduced to half for light from cascade emission sources. J.G. Rarity and P.R. Tapster[14] delved into the application of two-photon interference in the context of the Bell test experiment. Their work extended the fundamental principles established by Hong, Ou, and Mandel, focusing on utilizing two-photon interference for testing quantum nonlocality.

Two-photon interference, commonly referred to as the Hong-Ou-Mandel (HOM) effect, is a fundamental phenomenon in quantum optics. Figure 2 shows a schematic of the experimental setup for the HOM experiment[15]. The HOM effect occurs when two indistinguishable photons enter a BS from two different input ports (ports 2, and 3 in Fig. 2), leading to interference that results in the photons being detected at the same output port (either port 4 or 5 in Fig. 2), even though classical physics would predict otherwise. This two-photon interference with a balanced BS can be derived using quantum mechanical formalism.

2.1 Theoretical Derivation for HOM Interference

Consider,two optical input modes (a,b), and two output modes (c,d) of a lossless $50-50$ BS. $(a, a^\dagger)$, $(b, b^\dagger)$, $(c, c^\dagger)$, and $(d, d^\dagger)$ are the annihilation and creation operators in the BS modes, such that,

$$|1; j\rangle_a |1; k\rangle_b = a_j^\dagger b_k^\dagger |0\rangle_a |0\rangle_b,$$

where j, and k are photon's properties which determine how distinguishable they are. The transformation of a state during its interference on a BS can be described using a unitary operator. This operator governs the evolution of the creation operators as $a^\dagger \rightarrow \frac{c_j^\dagger + d_j^\dagger}{\sqrt{2}}$ and $b^\dagger \rightarrow \frac{c_k^\dagger - d_k^\dagger}{\sqrt{2}}$.

The output state is,

$$\begin{aligned} |\psi_{HOM}\rangle &= \frac{c_j^\dagger + d_j^\dagger}{\sqrt{2}} \frac{c_k^\dagger - d_k^\dagger}{\sqrt{2}} |0\rangle_c |0\rangle_d \\ &= \frac{1}{2}\left(c_j^\dagger c_k^\dagger - c_j^\dagger d_k^\dagger + d_j^\dagger c_k^\dagger - d_j^\dagger d_k^\dagger\right) |0\rangle_c |0\rangle_d \end{aligned} \tag{9}$$

If all the properties of the photon pair are identical ($j = k$), then the second and fourth terms in Eq. 9 cancel out. Therefore, the output state is,

$$|\psi_{HOM}\rangle = \frac{1}{\sqrt{2}}(|2\rangle_c |0\rangle_d - |0\rangle_c |2\rangle_d) \tag{10}$$

The state is still normalized because $a^\dagger |n\rangle = \sqrt{n+1}\,|n+1\rangle$.

If the two photons are completely indistinguishable, the probability of detecting a coincidence at the output ports of the BS is 0. However, if the photons are distinguishable, the second and third terms in Eq. 9 do not cancel out. As a result, the output state is given by,

$$|\psi_{dis}\rangle = \frac{1}{2}(|2\rangle_c |0\rangle_d - |1\rangle_c |1\rangle_d + |1\rangle_d |1\rangle_c - |0\rangle_c |2\rangle_d) \tag{11}$$

The probability of coincidence is $|\frac{1}{2}|^2 + |-\frac{1}{2}|^2 = \frac{1}{2}$.

As the time delay (τ) between the photons is varied, the coincidence detection rate shows a dip at zero delay, which is a signature of the HOM effect. The depth of this dip serves as a key indicator of the quantum nature of the light source and the degree of indistinguishability between the

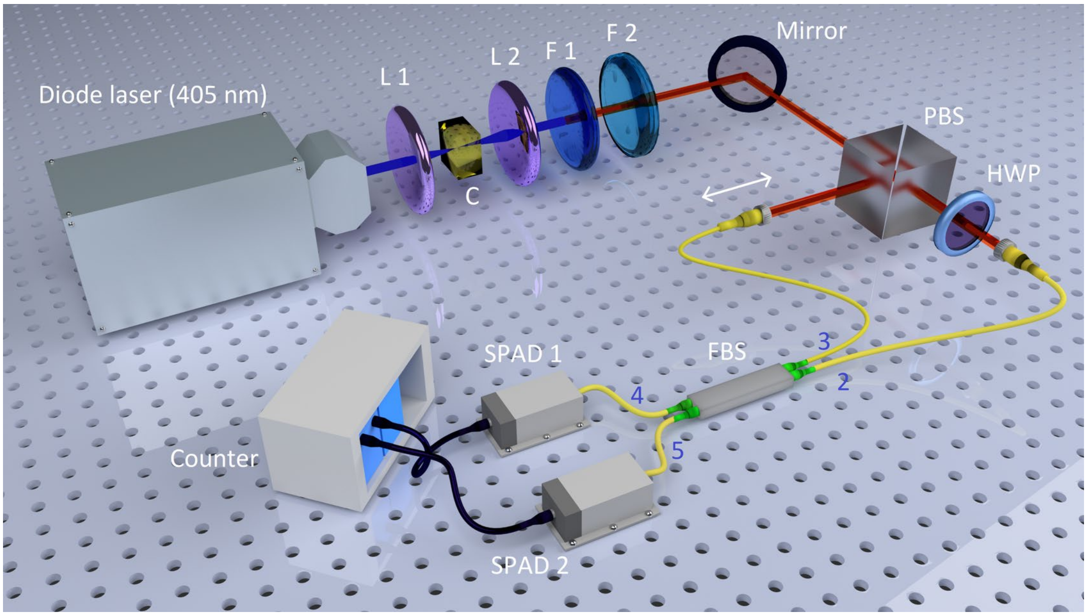

Figure 2 Illustration of the HOM experimental setup, adapted from[15]. A diode laser generates a coherent pump beam at 405 nm wavelength, which falls on a type II BBO crystal (C). A pair of lenses (L1) and (L2) is used to focus the pump beam at the crystal and to collimate the beam, respectively. The polarization of the pump beam is maintained as horizontal (H). The crystal is tilted such that the collinear phase matching condition is satisfied. In this configuration, down-conversion creates pairs of orthogonally polarized, frequency-degenerate photons at 810 nm wavelength. A long-pass filter (F1) blocks the pump beam (405 nm) and passes only the single-photon pairs (810 nm). A band-pass filter (F2) with a 3.1 nm bandwidth centred on 810 nm restricts the bandwidth of the transmitted photons and minimize any distinguishability in spectral degree of freedom. Two photons with orthogonal polarization, in any pair, are split in two directions by a polarizing beam splitter (PBS). Again, a half-wave plate (HWP) in one of the output arms of the PBS is used to make both photons the same polarized. Two fiber-couplers collect photons from the same pair in two single-mode fibers; in order to maintain indistinguishability in spatial degree of freedom, and inject them in a 2×2 polarization maintaining, fused fiber beam-splitter (FBS). One of the couplers is mounted on a motorized stage, which translates along the direction of the beam, to set a variable delay $\delta\tau$ between the two photons. After passing through the FBS, photons are detected in two single-photon avalanche detectors (SPAD), which are connected to a single-photon counting module; in order to perform coincidence measurement.

photon pair. This measure is referred to as the visibility of the interference.

Based on the discussion above, the probability of coincidence at the output ports of the BS is $\frac{1}{2}$ when $j \neq k$ and 0 when $j = k$, the visibility of the HOM dip can be expressed as,

$$V_{HOM} = \frac{p(\tau = \infty) - p(\tau = 0)}{p(\tau = \infty) + p(\tau = 0)}, \tag{12}$$

, where $p(\tau)$ represents coincidence probability, given by,

$$p(\tau) = \frac{1}{2}[1 - \delta(\tau)], \tag{13}$$

where $\delta(\tau)$ is defined as $\delta(\tau) = 1$ at $\tau = 0$ and $\delta(\tau) = 0$ otherwise.

In this context, it is important to note that practical simultaneous detection is limited by a finite time window. If two signals arrive within this defined interval, they are regarded as arriving simultaneously. This interval is known as the coincidence window.

Here, the indistinguishability between the pair of photons encompasses their spectral, polarization, and temporal overlap. If the arrival times of the two photons at the 50 : 50 BS differ, a temporal delay τ is introduced between them. This delay causes the temporal mode functions of the two photons to no longer perfectly overlap. In the operator formalism, the creation operators acquire temporal dependence:

$a_j^\dagger \to a_j^\dagger(t)$ and $b_k^\dagger \to b_k^\dagger(t+\tau)$. Using thes, the output state becomes

$$|\psi_{HOM}\rangle = \frac{1}{2}\Big(c_j^\dagger(t)c_k^\dagger(t+\tau) - c_j^\dagger(t)d_k^\dagger(t+\tau) + d_j^\dagger(t)c_k^\dagger(t+\tau) - d_j^\dagger(t)d_k^\dagger(t+\tau)\Big)\ |0\rangle_c\,|0\rangle_d \tag{14}$$

If $\tau = 0$ and $j = k$, the operators $c_j^\dagger(t)$ and $c_k^\dagger(t+\tau)$ (and similarly for the d mode operators) act on the same temporal mode. In that case, the second and third terms have the same magnitude but opposite sign, leading to a commutation-like cancellation. However, if $\tau \neq 0$ even when $j = k$, the creation operators act on different temporal modes due to the delay. As a result, the cancellation of the second and third terms is no longer perfect. To quantify the partial cancellation, the temporal mode functions $\phi_j(t)$ and $\phi_k(t+\tau)$ are introduced. These functions describe the temporal profile of the photon wavepackets at times t and $t+\tau$, respectively, and satisfy the normalization condition: $\int |\phi_j(t)|^2 dt = 1$. For simplicity, these functions can be assumed to have a Gaussian profile. The operators act on these envelopes of wavepackets as: $a_j^\dagger(t) = \phi_j(t)\, a_j^\dagger$ and $b_k^\dagger(t+\tau) = \phi_k(t+\tau)\, b_k^\dagger$. The degree of cancellation between the second and third terms in Eq. 14 depends on the overlap of the temporal mode functions: $\langle\phi_j|\phi_k\rangle = \int \phi_j^*(t)\,\phi_k(t+\tau)dt$. At $\tau = 0$, $\phi_j(t) = \phi_k(t)$, so the overlap is 1, leading to perfect cancellation of the second and third terms in Eq. 14. At $\tau \neq 0$, the overlap decreases. Consequently, the coincidence probability in Eq. 13 is modified to:

$$p(\tau) = \frac{1}{2}[1 - |\langle\phi_j|\phi_k\rangle|^2] \tag{15}$$

.

2.2 *Spectral Distingushability*

In practice, the incident photons are not perfectly monochromatic, meaning the two photons are not spectrally identical and possess a spectral width σ_ω. As a result, Eq. 13 is modified by,

$$p(\tau) = \frac{1}{2}[1 - e^{\sigma_\omega^2\,\tau^2}] \tag{16}$$

The spectral amplitudes of the two photons can be correlated, as observed in parametric down-conversion processes. This spectral correlation is described by the joint spectral amplitude $f(\omega_1, \omega_2)$, where ω_1, and ω_2 represent the central frequencies of the two incident photons. The coincidence probability in this scenario has been both theoretically and experimentally demonstrated, as shown in[16], and is given by,

$$p(\tau) = \frac{1}{2}\left(1 - \int_0^\infty \int_0^\infty d\omega_1\, d\omega_2\, |f(\omega_1, \omega_2)|^2\, e^{i(\omega_1 - \omega_2)\tau}\right) \tag{17}$$

The spectral function, $f(\omega_1, \omega_2)$ can be modified by applying a bandpass filter. Typically, the filter function can be approximated by a sinc function, which results in a bump in the wings of the HOM dip as shown in Fig. 3.

Spectral and temporal distinguishability in multi-photon interference has been explored both theoretically and experimentally, and HOM dips have been observed with different degrees of visibility, depending on the level of indistinguishability achieved in different experimental scenarios, in the ref.[17–31].

Furthermore, the variation in the visibility with the pump power in parametric down-conversion has been studied both theoretically and experimentally for type I and type II phase-matching crystals in[32].

2.3 *Application of HOM Interference*

2.3.1 Manifestation of Quantumness

A 50% visibility in the HOM dip is generally regarded as the threshold distinguishing classical from quantum behavior of light. When two classical beams with equal intensities and randomly varying relative phase are incident on a 50:50 BS, the maximum achievable HOM dip visibility is limited to 50%[33]. However, in[15], an experiment demonstrated that nearly 100% visibility in the HOM dip can be achieved even with classical fields. In the semiclassical framework of photodetection theory, the coincidence probability is proportional to the cross-correlation of the integrated intensities at the detectors. The normalized correlation function $C(\tau)$ is derived, and it is shown that the visibility of the coincidence dip, denoted as V, depends on the fluctuation probability distribution of the relative phase ϕ between the input pulses. To further elaborate, the phase fluctuations between the input fields are critical in determining the visibility of the HOM dip. In the context of this experiment, the phase is treated as a random variable, and its fluctuation is captured by a fixed probability distribution $P(\phi)$. The probability distribution is chosen such that the average fluctuation of the phase, when weighted by $P(\phi)$, does not introduce a bias, which requires $\int P(\phi)\cos\phi\ d\phi = 0$. This ensures that the cosine

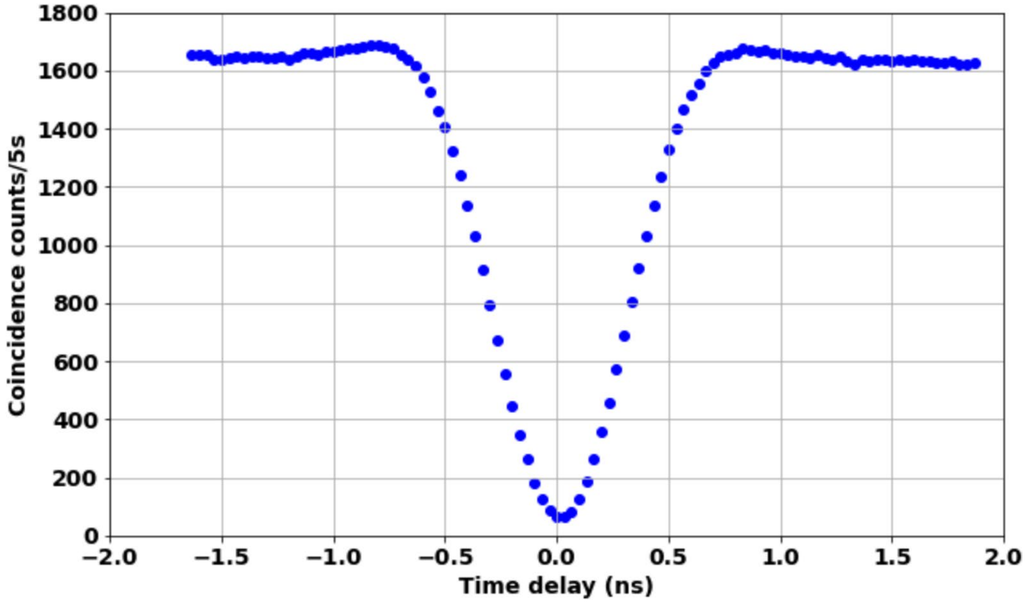

Figure 3 An example of a HOM dip, where the coincidence counts are plotted as a function of the path delay between two photons, is achieved in the experimental setup presented in Fig 2[15]. The data acquisition time is 5 seconds, and for each time delay the measurement is repeated 100 times to improve averaging. Blue points represent the experimental mean.

function's average value over all phase values is zero. This condition effectively represents a uniform distribution of phase fluctuations without a net phase shift. Therefore, V is expressed as,

$$V = \int P(\phi) \cos^2 \phi \; d\phi \tag{18}$$

When the relative phase ϕ is uniformly randomized over $[0, 2\pi]$, Eq. 18 shows that the V reaches the classical limit of 50%. However, with controlled phase distributions, such as $[0, \pi]$, V can reach 100%, even with classical pulses. This demonstrates that the classical upper limit of 50% arises from a lack of phase control rather than being an inherent boundary of classical electromagnetic field theory.

The experiment employs an electrical system where phase control is directly achieved through an arbitrary waveform generator. Two Gaussian amplitude-modulated sine waves, generated by the waveform generator, are input to a balanced BS (power splitter) with carrier frequencies and relative phases controlled to ensure identical inputs. The system's components, including mixers, oscilloscopes, and power splitters, are calibrated for optimal performance. The time delay between the two input signals is varied systematically, and the cross-correlation of the outputs is analyzed to determine visibility. With phase values restricted to $[0, \pi]$, with equal probability, the experiment achieves a visibility of 99.63%.

To further distinguish between quantum and classical behavior, a complementarity test was conducted by introducing an additional BS into the setup, effectively constructing a Mach-Zehnder interferometer with a phase shifter. The experiment was carried out in two scenarios: In Case I, both input arms of the second BS were open, while in Case II, one of the input arms was blocked. In Case I, both arms of the interferometer are unblocked, and the second BS recombines the photon paths. In the classical scenario, the output from the first BS enters both arms, resulting in an interference pattern with a 100% correlation. In the quantum scenario, the photons are in a superposition state, and the system behaves similarly, also showing a 100% coincidence. In Case II, in the classical scenario, when one arm of the interferometer is blocked, it effectively blocks half of the signal. The unblocked arm is then split into two, resulting in a 50% cross-correlation compared to Case I, as the beam is only partially recombined. In the quantum scenario, when one arm is blocked, the superposition state collapses to one of two possibilities: $|0, 2\rangle$ or $|2, 0\rangle$, each with equal probabilities. After passing through the second BS, the output state is given by: $\frac{1}{2}|0, 2\rangle + \frac{1}{2}|2, 0\rangle + \frac{1}{\sqrt{2}}|1, 1\rangle$. This results in a coin-

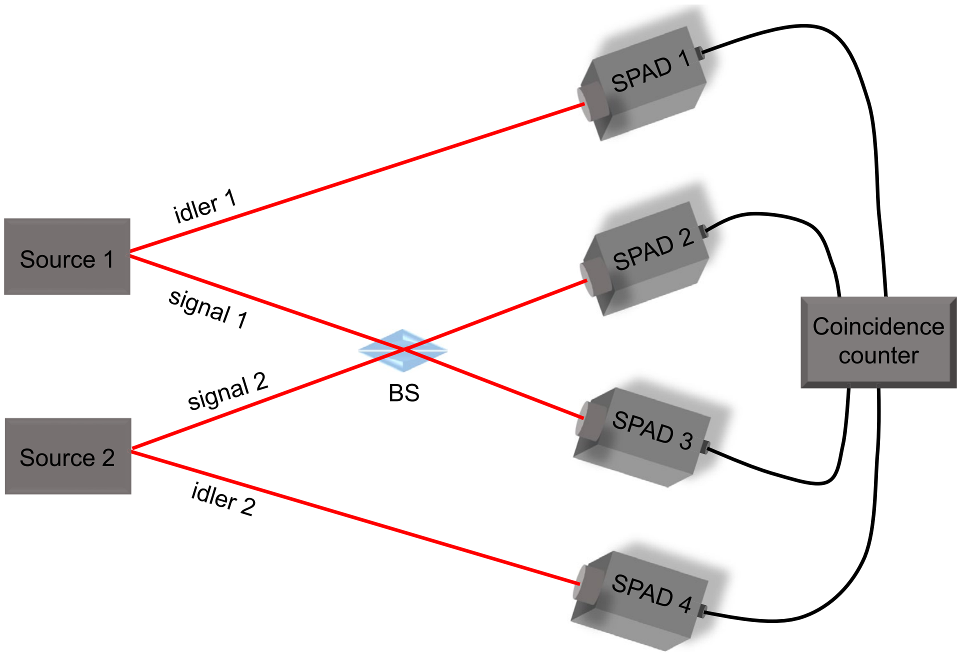

Figure 4 The schematic illustrates the experimental setup for HOM interference between two photons originating from two distinct single-photon sources (source 1 and source 2). Signal photons (s1 and s2) from each source interfere at the BS, while the corresponding idler photons (i1 and i2) are used for heralding. Four single-photon detectors (SPADs) are employed to measure photon counts, and a coincidence counter records the four-fold coincidence events.

cidence probability of $\frac{1}{2}$. The decrease in coincidence probability, combined with the blocking of half of the superposition states, leads to a 25% coincidence rate compared to Case I.

In[34], the quantum and classical aspects of the HOM experiment were analyzed, presenting a general expression for intensity correlations that clearly highlights the differences between a classical HOM-like dip and a quantum one.

2.3.2 Indicator of Indistinguishability

The visibility of a HOM dip is a critical measure of the indistinguishability of input photons. Two photons are considered indistinguishable if they share the same electromagnetic field mode, meaning they have identical polarization, frequency, arrival time, and spatial profile. When photons are perfectly indistinguishable, the HOM visibility approaches 1. This phenomenon is commonly used to assess the mode indistinguishability of photons generated through SPDC[9,12,14]. However, HOM interference is not limited to SPDC-generated photons. It can also be applied to single photons produced by other physical systems, such as quantum dots and vacancy centers, to evaluate their indistinguishability[35–37].

HOM interference can also occur between two photons originating from independent sources–one from source 1 and the other from source 2. This type of interference is crucial for quantum communication protocols, such as quantum teleportation. Figure 4 illustrates a general schematic of the experimental setup. Here, signal photons (s1 and s2) from both sources are directed to the two input ports of a BS, while the corresponding idler photons (i1 and i2) are used for heralding. In this scenario, Eq. 17 is modified to reflect the four-fold coincidence probability[38].

The four-fold coincidence, $p_4(\tau)$ can be expressed as a function of the time delay τ,

$$p_4(\tau) = \frac{1}{4}\int_0^\infty\int_0^\infty\int_0^\infty\int_0^\infty d\omega_{s1}\,d\omega_{i1}\,d\omega_{s2}\,d\omega_{i2}\,|f_1(\omega_{s1},\omega_{i1})f_2(\omega_{s2},\omega_{i2}) - f_1(\omega_{s2},\omega_{i1})f_2(\omega_{s1},\omega_{i2})\,e^{-i(\omega_{s2}-\omega_{s1})\tau}|^2 \tag{19}$$

For 100% visibility, at $\tau = 0$, $p_4(\tau)$ must be 0. As demonstrated by Eq. 19, this condition is satisfied if, $f_1(\omega_{s1},\omega_{i1})f_2(\omega_{s2},\omega_{i2}) = f_1(\omega_{s2},\omega_{i1})f_2(\omega_{s1},\omega_{i2})$. This condition is met when the two joint spectral amplitudes are identical.

$$f_1(\omega_{s1},\omega_{i1}) = f_2(\omega_{s2},\omega_{i2}) \tag{20}$$

Additionally, both functions must be separable such that they can be expressed as a product of independent components.

$$f(\omega_s, \omega_i) = \mathcal{F}_s(\omega_s)\mathcal{F}_i(\omega_i) \tag{21}$$

Eq. 20 indicates that the two sources emit indistinguishable photons and Eq. 21 indicates that the sources are spectrally pure, meaning that the photons emitted by the sources have well-defined spectral properties, such as a narrow bandwidth and a single frequency component. The integral in Eq. 19 is evaluated only for the signal photons, as they contribute to the HOM interference. Equation 19 exclusively for the signal photons,

$$p_4(\tau) = \frac{1}{4}\int_0^\infty \int_0^\infty d\omega_{s1}\, d\omega_{s2}\, |\mathcal{F}_{s1}(\omega_{s1})\mathcal{F}_{s2}(\omega_{s2}) - \mathcal{F}_{s1}(\omega_{s2})\mathcal{F}_{s2}(\omega_{s1})e^{-i(\omega_{s2}-\omega_{s1})\tau}|^2 \tag{22}$$

The photon spectra are considered as normalized Gaussian functions $(\mathcal{F}_s(\omega_s) = \sqrt{\frac{2}{\pi\,\sigma_s^2}}\exp[-(\frac{\omega_s-\omega_{s0}}{\sigma_s})^2])$. After integration Eq. 22 simplifies to,

$$p_4(\tau) = \frac{1}{2} - \frac{\sigma_{s1}\,\sigma_{s2}}{\sigma_{s1}^2+\sigma_{s2}^2}\, exp\left[-\left(\frac{\sigma_{s1}^2\,\sigma_{s2}^2\,\tau^2 + 4(\omega_{s20}-\omega_{s10})^2}{2(\sigma_{s1}^2+\sigma_{s2}^2)}\right)\right], \tag{23}$$

where ω_{s10} and ω_{s20} represent the central frequencies of the photons, while σ_{s1} and σ_{s2} denote their respective bandwidths. Equation 23 shows that as the central frequencies of the photons deviate from each other, the visibility of the HOM dip decreases. Similarly, if the bandwidth of one photon becomes larger than that of the other, the visibility also diminishes.

HOM interference experiments between two photons generated from independent sources have been demonstrated, including experiments with two photons generated by two separate SPDC sources, as well as experiments involving one single photon generated by SPDC and one from a weak coherent pulse. In this setup, one of two configurations is typically used to generate the pump wavelength required for SPDC. In the first configuration, a mode-locked titanium-sapphire laser serves as the master laser. The laser output undergoes frequency doubling to produce the desired pump wavelength, which is then split by a BS. The reflected beam pumps one nonlinear crystal, while the transmitted beam pumps the second crystal, effectively creating two independent SPDC sources[39]. Using this setup, HOM visibility as high as 94% has been achieved, demonstrating the high level of indistinguishability between the two independent sources[40]. Alternatively, the two nonlinear crystals can be pumped sequentially by directing the beam through both crystals[41]. These configurations ensure that both crystals are pumped by the same master laser, maintaining coherence between the two-photon sources. Alternatively, in the second configuration, two independent titanium-sapphire lasers are used to pump the two SPDC sources. To ensure synchronization between the laser pulses, an electronic feedback mechanism is employed[42].

If one of the sources is a weak, coherent pulse, the setup is slightly modified. In this case, a BS is placed in the path of the titanium-sapphire laser beam. One of the split beams serves as the weak coherent pulse source after being attenuated by a filter, while the other beam is directed towards the nonlinear crystal for SPDC after undergoing frequency doubling.[33]. In this configuration, three-fold coincidence counts are typically measured to plot the HOM dip. Visibility as high as 89% has been achieved[43].

In those cases, it is important to ensure that the two photons arrive at the BS simultaneously. To achieve this, an optical path delay may need to be introduced into the photon paths within the experimental setup. This adjustment compensates for any difference in travel distance, thereby aligning the arrival times and optimizing the interference visibility.

Haldar et al. demonstrated two-photon interference between two independent SPDC sources, where each crystal was pumped by a continuous-wave laser[44]. A key requirement for this interference is that the detection times must be measured with a precision finer than the coherence time of the photons. Since single-photon detectors inherently exhibit minimal jitter, the coherence time of the photons must be extended to surpass this jitter. This is achieved by applying narrow spectral filtering. In their experiment, a highly narrow bandpass filter with a bandwidth of 10 picometers was used to ensure sufficient coherence.

Two-photon interference between independent single-photon sources has been demonstrated beyond SPDC. This includes interference between photons emitted from two vacancy centers within a nanodiamond[45,46] or from two remotely positioned nanodiamonds[47,48], as well as between two quantum dots[49]. Additionally, two-photon interference has been achieved using photons retrieved from two separate quantum memories[50,51]. These demonstrations highlight

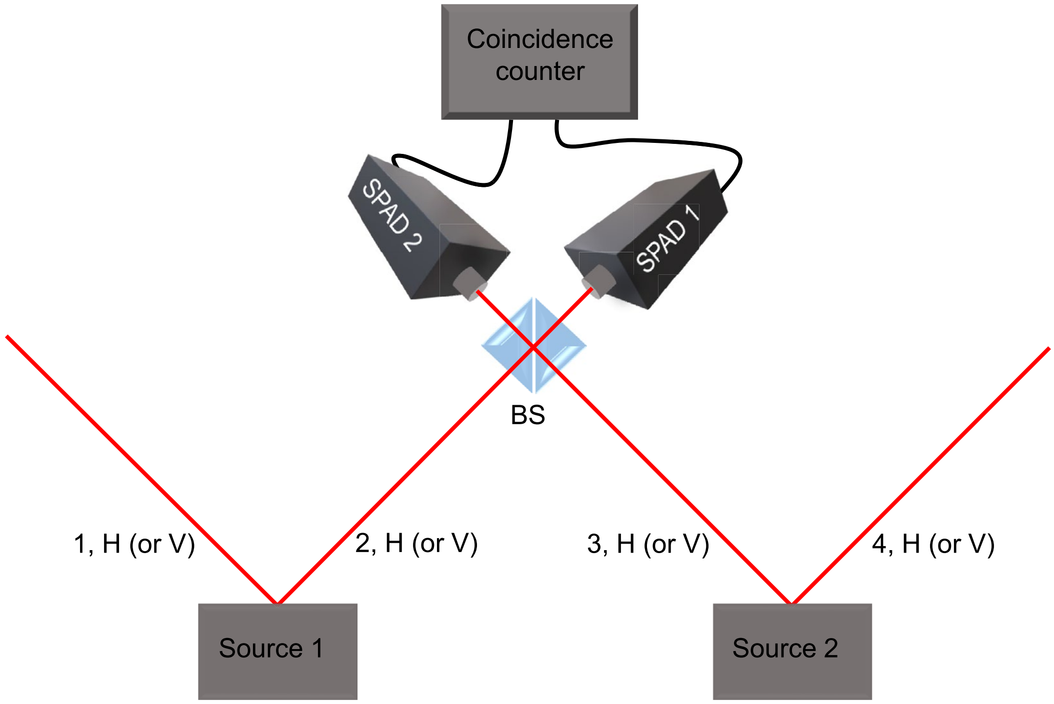

Figure 5 The schematic illustrates the experimental setup for BSM.

the versatility of HOM interference across various quantum systems.

2.3.3 Entanglement-Based Communication

Entanglement is a crucial element of quantum communication. Entanglement is generated by either producing two entangled particles from the same source or through direct interaction between particles. However, entanglement can also be established through a process known as entanglement swapping, which leverages the projection of two particles onto an entangled state. Notably, this approach does not necessitate any physical interaction between the particles involved. Instead, if each particle is already entangled with another partner, performing a measurement, such as a Bell-state measurement, on the partner particles can project the remaining two particles into an entangled state. This remarkable manifestation of the projection postulate forms the foundation of entanglement swapping[52,53].

A Bell-state measurement (BSM) is a process that projects two particles onto one of four maximally entangled states, known as Bell states. This measurement is essential for entanglement swapping as it determines the final entangled state of the remaining particles (Fig. 5). The physical mechanism behind BSM often relies on two-photon interference, a phenomenon where two indistinguishable photons interfere destructively or constructively depending on their relative phase and polarization. When two photons arrive simultaneously at a beam splitter, the interference pattern generated dictates the projection onto a specific Bell state. By harnessing this interference, BSM can effectively entangle distant particles, making it a key ingredient in entanglement distribution protocols[54,55]. BSM plays a vital role in quantum teleportation[56]

Consider two single-photon sources. The first source generates an entangled photon pair, where both photons are either horizontal (HH) or vertical (VV) polarized, denoted as photons 1 and 2 with the state $|\psi_1\rangle = \frac{1}{\sqrt{2}}(|HH\rangle_{12} + |VV\rangle_{12}$.

The second source generates a similar entangled photon pair, also either HH or VV polarized, denoted as photons 3 and 4 with the state $|\psi_1\rangle = \frac{1}{\sqrt{2}}(|HH\rangle_{34} + |VV\rangle_{34}$. Thus, the total state

of the system (photons 1, 2, 3, and 4) is the combined state of the two entangled pairs:

$$\begin{aligned}|\psi_{total}\rangle &= |\psi_1\rangle \otimes |\psi_2\rangle \\ &= \frac{1}{2}(|HH\rangle_{12} + |VV\rangle_{12})\otimes \\ &\quad (|HH\rangle_{34} + |VV\rangle_{34})\end{aligned} \tag{24}$$

Photons 2 and 3 undergo BSM, where they interfere on a balanced beam splitter. The BSM projects the state of photons 2 and 3 onto one of the four Bell states:

$$|\phi^{+}\rangle = \frac{1}{\sqrt{2}}(|HH\rangle + |VV\rangle)$$

$$|\phi^{-}\rangle = \frac{1}{\sqrt{2}}(|HH\rangle - |VV\rangle)$$

$$|\psi^{+}\rangle = \frac{1}{\sqrt{2}}(|HV\rangle + |VH\rangle)$$

$$|\psi^{-}\rangle = \frac{1}{\sqrt{2}}(|HV\rangle - |VH\rangle)$$

Now, considering the total state of photons 1, 2, 3, and 4, we can rewrite it in terms of the Bell states. If photons 2 and 3 are projected into the $|\phi^{+}\rangle$ state, the total state collapses to:

$$|\psi_{total}\rangle = \frac{1}{2}(|\phi^{+}\rangle_{23}) \otimes (|HH\rangle_{14} + |VV\rangle_{14}) \tag{25}$$

This process results in photons 1 and 4 becoming entangled. The final entangled state between photons 1 and 4 is, $|\psi\rangle_{14} = \frac{1}{\sqrt{2}}(|HH\rangle_{14} + |VV\rangle_{14})$. If photons 2 and 3 are measured in the $|\phi^{-}\rangle$ state, the result is $|\psi\rangle_{14} = \frac{1}{\sqrt{2}}(|HH\rangle_{14} - |VV\rangle_{14})$. Therefore, the entanglement-swapping process depends on the BSM outcome.

Entanglement swapping plays a critical role in developing quantum repeater networks, which are essential for extending the range of quantum communication. In a quantum repeater architecture, quantum memories are distributed along a communication channel, with each memory holding two atoms capable of emitting photons in opposite directions. A Bell-state analyzer positioned midway between two adjacent memories detects the photons travelling from each memory, performing a BSM to establish entanglement between the atoms stored in the two memories. By repeating this process across successive links, entanglement can gradually be extended across multiple memories, effectively connecting distant locations. Once successful, this chain of entanglement enables the creation of entangled pairs between the first and final nodes of the network, facilitating secure quantum communication over long distances[57–59]. A detailed and comprehensive exploration of entanglement swapping in quantum repeater network architecture would warrant a separate review paper. Readers are encouraged to refer to[60,61] for further information.

2.3.4 Signature of Precision

As previously mentioned, the HOM dip serves as a key indicator of photon indistinguishability. It provides a means to quantify the optical delay between two photons. The width of the HOM dip is inherently broad, and this width can be precisely controlled, making it particularly effective for detecting and measuring small optical delays. The control over the HOM dip width allows for fine-tuning of the system to improve precision in timing measurements. In the case of SPDC, the width of the HOM dip can be adjusted by varying the crystal length[62]. Additionally, the bandwidth of the bandpass filter can also be adjusted to control the HOM dip width[63]. In a common-path HOM setup described in[64], researchers successfully measured the group delay of photons with an impressive precision of 0.1 femtoseconds and the phase delay with a precision of 8 attoseconds. Further advancements in precision measurement were introduced by Lyons et al. in their work on attosecond-resolution HOM interferometry[63]. They devised a measurement strategy based on Fisher information analysis, which enabled the team to achieve an accuracy of 0.5 attoseconds.

The HOM dip can be effectively applied to measure and control the group velocity of photons by manipulating their transverse profiles. By structuring the signal photon's wavefront using spatial light modulators, it is possible to induce changes in the photon's group velocity. This is achieved by altering the transverse spatial characteristics of the photon, such as its wavefront shape. After the photon travels through free space, a second Spatial light modulator is used to reverse the wavefront modification, thereby restoring the photon to its original state. The interference between the structured signal photon and the idler photon, when both are directed onto a balanced BS, produces the HOM dip. Importantly, when the group velocity of the signal photon is changed, the HOM dip shifts. This shift in the HOM dip directly corresponds to a time delay, providing a clear measurement of the change in the photon's group velocity[65].

An experiment described in[66] further demonstrates this concept. The researchers showed that a change in the orbital angular momentum of a photon introduces a time shift in the HOM dip. By modifying the orbital angular momentum of the signal photon, the HOM dip undergoes a shift, effectively linking the photon's orbital angular momentum to a temporal delay. This highlights the potential of HOM interference as a powerful tool for measuring and controlling photon velocities.[67] identifies an optimal scaling relationship between the precision and visibility of the HOM dip. Therefore, HOM interference can be used in quantum metrology to achieve measurements with exceptionally high precision, thus opening a new regime in precision measurement techniques. However, the detailed discussion on this topic, including its applications and theoretical framework, is outside the scope of this review paper. For further reading, readers are advised to refer to[68].

Optical Coherence Tomography (OCT) is an imaging technique used for depth profiling of tissue samples. It works by measuring the interference between light reflected from the sample and a reference beam. In practice, this technique is limited by the coherence of the light source and the dispersion of the sample. In this context, HOM interference offers a significant improvement. To overcome the limitations, a technique called Quantum Optical Coherence Tomography (QOCT) has been proposed. This technique leverages the automatic dispersion cancellation inherent in the two-photon interference effect[69]. Additionally, QOCT offers a twofold improvement in resolution compared to classical OCT. In the experimental setup, the sample is placed in one arm of the HOM interferometer, and coincidence counts are recorded while varying the path of the other arm using a translation stage. Shortly after its proposal, QOCT was experimentally demonstrated, achieving a fivefold improvement in resolution compared to OCT[70]. Various experiments using different techniques have achieved even better depth resolution. However, a detailed discussion of these experiments is beyond the scope of this review. For further information, readers are advised to consult[71].

3 Multiple Photon Path Interference

3.1 Interference and Sum Rule

In his seminal paper[72] Rafael D. Sorkin examines how interference emerges as a consequence of the failure of classical probability additivity. It introduces a hierarchy of sum rules, where the second sum rule corresponds to classical probability and ensures no interference. However, quantum probabilities obey a weaker condition where interference terms persist. The second sum rule refers to the classical additivity of probabilities:

$$P(A \cup B) = P(A) + P(B) \tag{26}$$

for mutually exclusive events A and B. In classical probability theory, this always holds, meaning there is no interference between different paths or events. However, in quantum mechanics, probabilities do not always sum linearly due to interference effects. The deviation from this classical additivity is captured by an interference term:

$$I(A, B) = P(A \cup B) - P(A) - P(B) \tag{27}$$

To derive the third-order sum rule for a triple-slit experiment, the Born rule and the superposition principle are used. According to the Born rule, the probability of an event is given by the squared modulus of the wavefunction: $P(X) = |\psi(X)|^2$. For a particle passing through slits A, B, and C, the total wavefunction is the sum of contributions from each slit: $\psi_{A,B,C} = \psi_A + \psi_B + \psi_C$. For two slits A and B, the probability is: $P(A \cup B) = |\psi_A + \psi_B|^2$. Expanding using the Born's rule, the above equation becomes,

$$P(A \cup B) = |\psi_A|^2 + |\psi_B|^2 + 2\mathcal{R}(\psi_A^* \psi_B) \tag{28}$$

Here, $\mathcal{R}(\psi_A^* \psi_B)$ is the interference term between slits A and B. Similarly, for other pairs:

$$P(B \cup C) = |\psi_B|^2 + |\psi_C|^2 + 2\mathcal{R}(\psi_B^* \psi_C) \tag{29}$$

$$P(A \cup C) = |\psi_A|^2 + |\psi_C|^2 + 2\mathcal{R}(\psi_A^* \psi_C) \tag{30}$$

For all three slits open:

$$\begin{aligned} &P(A \cup B \cup C) \\ &\quad = |\psi_A + \psi_B + \psi_C|^2 = |\psi_A|^2 + |\psi_B|^2 + |\psi_C|^2 \\ &\qquad + 2\mathcal{R}(\psi_A^* \psi_B) + 2\mathcal{R}(\psi_B^* \psi_C) + 2\mathcal{R}(\psi_A^* \psi_C) \end{aligned} \tag{31}$$

The third-order interference term is defined as:

$$\begin{aligned} &I(A, B, C) \\ &\quad = P(A \cup B \cup C) - P(A \cup B) \\ &\qquad - P(B \cup C) - P(A \cup C) + P(A) + P(B) + P(C) \end{aligned} \tag{32}$$

Substituting Eqs. 31,30,29,and 28 in Eq. 32, and expanding all terms, $I(A, B, C) = 0$. Therefore, $I(A, B, C) = 0$ serves as a test for the validity of the Born rule. In this context, the Sorkin parameter quantifies any deviation from the expected quantum probability sum, measuring the extent to which the observed probability differs from the classical sum of individual slit probabilities.

In[73], the authors have conducted a three-slit experiment with photons to test the validity of Born's rule by investigating the presence of third-order interference. They measured the quantity ϵ, defined as

$$\begin{aligned}\epsilon = P_{ABC} - (P_{AB} + P_{AC} + P_{BC}) \\ + (P_A + P_B + P_C) - P_0\end{aligned} \tag{33}$$

where P_{ABC} is the probability of detection when all three slits are open, P_{AB}, P_{AC}, P_{BC} are probabilities when two slits are open, P_A, P_B, P_C correspond to single-slit openings, and P_0 accounts for background noise (probability of detection when all slits are closed). To compare any possible deviation from the rule, the study defines a normalized quantity: $\kappa = \frac{\epsilon}{\delta}$, where δ is defined as,

$$\begin{aligned}\delta &= |I_{AB}| + |I_{AB}| + |I_{AB}| \\ &= |P_{AB} - P_A - P_B + P_0| + |P_{BC} - P_B - P_C + P_0| \\ &+ |P_{AC} - P_A - P_C + P_0|\end{aligned}$$

If $\kappa = 0$, Born's rule holds perfectly, whereas $\kappa \neq 0$ suggests a deviation from it. The experiment employed an optical setup with a triple-slit, where each slit could be selectively opened or blocked using a blocking mask, with slit combinations chosen randomly to minimize systematic errors. Various types of photon sources were used, and the interference patterns were recorded using SPADs. By analyzing photon intensities across all slit configurations (single-, double-, and triple-slit cases), the researchers established an upper bound on three-path interference, limiting it to less than $10^{-}2$ of the expected two-path interference for SPDC based single photons and constraining it to $10^{-}3$ for the attenuated coherent laser beam. The results were consistent with Born's rule, effectively ruling out higher-order interference with high precision.

Several experiments have since been conducted to test Born's rule. In[74] the authors present a different approach using a three-path interferometer to establish a tighter empirical upper bound on potential deviations. Unlike conventional slit-based setups, this experiment employs a transmission grating to generate three independent optical paths. Two paths pass through individually controlled phase plates, allowing precise phase adjustments. All three paths are then retroreflected using a common mirror. To separate the outgoing and incoming beams, the setup incorporates a double pass through a quarter-wave plate and a polarizing BS. To account for detector nonlinearity, the researchers model the response using a Poissonian light source and a nonlinearity equation, allowing them to predict and subtract systematic errors. By measuring and comparing the three-path interference pattern with theoretical predictions, they set a new upper bound on three-path interference: $< 0.0015 \pm 0.0029$. Improved precision was achieved[75] by using a stabilized five-path interferometer instead of a three-path setup, minimizing systematic errors such as detector nonlinearity and phase drift. Two diffractive BS were employed to create and recombine five independent paths, with shutter assemblies providing control over which paths were open. Phase plates, mounted on motorized rotation stages, were inserted in each path for precise phase control. Detector nonlinearity was modelled and calibrated by separately measuring response curves. The entire interferometer was enclosed and temperature-stabilized. This study set tighter upper bounds on higher-order interference at: $10^{-}3$. $\kappa = 0$ has also been measured in various systems beyond photonics, including matter wave, atomic tests, and nuclear magnetic resonance systems. However, these are beyond the scope of this review article.

3.2 Non-Zero Sorkin Parameter

A nonzero ϵ signals a departure from standard quantum mechanics, indicating the presence of third-order interference. However, a nonzero ϵ does not necessarily imply a violation of Born's rule. The double-slit experiment, a cornerstone of both optics and quantum mechanics, typically assumes the wave function with both slits open is the sum of the individual wave functions from each slit: $\psi_{AB} = \psi_A + \psi_B$. However, this assumption is mathematically inaccurate. The three scenarios mentioned above correspond to distinct boundary conditions, meaning that the superposition principle can only be applied as an approximation in these cases. This can be addressed by Feynman's path integral formalism. This formalism involves summing over all possible paths a particle can take through the two slits. It includes not only the near-straight trajectories from the source to the detector through either slit (green paths in Fig. 6), but also incorporates nonclassical paths, such as the looped ones shown in purple in Fig. 6. While these looped paths contribute much less to the total intensity at the detector compared to the straight-line paths, their effect is nonzero and finite[76]. These contributions lead to a modified wave function $\psi_{AB} = \psi_A + \psi_B + \psi_L$, where ψ_L represents the looped paths. The presence of nonclassical paths, as shown in Fig. 6, challenges

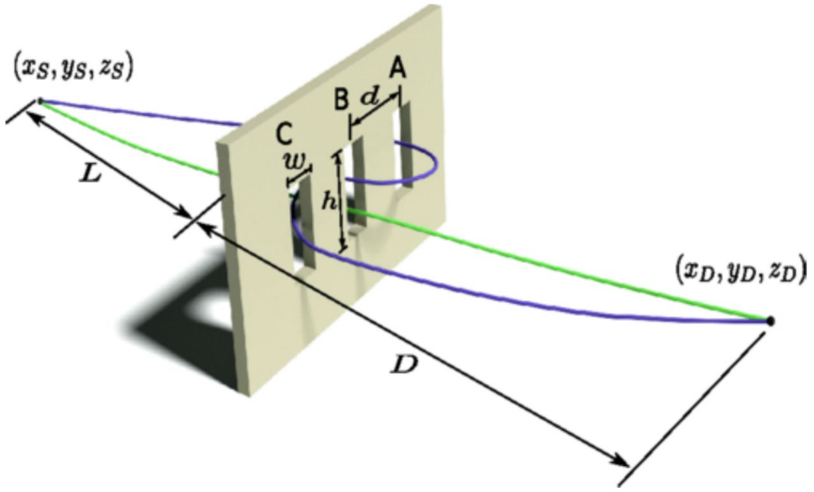

Figure 6 A point source is located at (x_s, y_s, z_s) at a distance L from a triple-slit system. Each slit has a width w, height h, and an inter-slit separation d. The detection point is at (x_d, y_d, z_d) situated at a distance D from the slit. The green path represents the classical trajectory, while the purple loops around the slits illustrate non-classical paths[76].

the conventional application of the superposition principle in interference experiments.

[76] suggests that the triple-slit experiment can be used to quantify the impact of nonclassical paths. These paths also affect the calculation of the experimentally measurable quantity κ, which has been used to set bounds on higher-order interference terms in quantum mechanics. κ exhibits modulation in its nonzero values as a function of the detector position. This means that if one plots the triple-slit interference pattern– intensity versus position– κ varies along the spatial coordinate. If only classical paths contributed to interference, κ would be zero. However, considering nonclassical paths allows for nonzero values of κ, indicating that a nonzero κ does not falsify Born's rule but instead supports the broader Feynman path integral formalism. The experiment in Ref.[73] did not detect the expected nonzero value of κ due to systematic errors. However, these errors can be corrected in future experiments, enabling more accurate measurements. Further analysis reveals that κ is highly sensitive to experimental parameters, and there is potential for larger κ values under certain conditions, such as increasing the wavelength of the photons.

An analytic formula has been derived to establish a bound on κ as a function of detector position in the far-field diffraction regime[77]. This formula has been verified against results from Finite Difference Time Domain simulations and numerical integration, demonstrating close agreement. The derived bound is: $|\kappa_{max}| \approx 0.03 \frac{\lambda^{\frac{3}{2}}}{d^{\frac{1}{2}} w}$, where λ is the wavelength of the light or particle used in the experiment.

The experimental verification of looped trajectories in a triple-slit interference experiment was achieved by enhancing electromagnetic near-fields around the slits using surface plasmons[78]. A nanostructured gold film with three slits in different opening configurations was fabricated to support surface plasmon excitation. A heralded single-photon source was used, and photon polarization was controlled with a half-wave plate and a polarizer to either excite surface plasmons (x-polarization) or suppress them (y-polarization). For x-polarization, the electric field oscillates parallel to the plane of the slits, inducing electron motion along the metal film and exciting surface plasmon waves. These plasmons enhances near-field interactions, increasing coupling between slits and amplifying the probability of looped trajectories. In contrast, for y-polarization, where the electric field oscillates perpendicular to the slit plane, surface plasmons are not excited, and only direct (classical) paths contributes, making looped trajectories negligible. As a result, the y-polarized interference pattern follows a standard three-slit distribution with no visible looped paths, while the x-polarized pattern shows significant deviations, with increased visibility due to interference between classical and looped trajectories. The probability ratios for x- and y-polarized photons varies across different slit configurations, confirming that looped paths

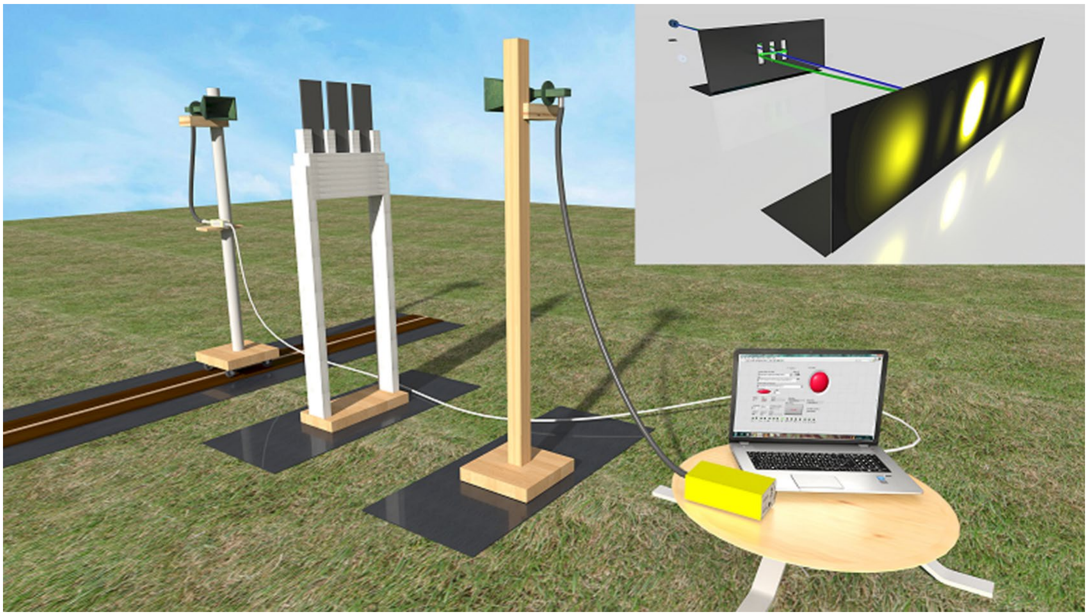

Figure 7 Schematic of the experimental setup in[79]. The green antennas on both sides are pyramidal horn antennas, serving as the source and receiver of electromagnetic waves at 5 cm wavelength. The receiving antenna is mounted on a movable rail, allowing for the measurement of diffraction patterns. Positioned between the source and receiver are three slots. The inset illustrates a triple-slit schematic, where the blue line represents a classically dominant path, while the green line depicts a sub-leading path within the path integral formalism.

influences the pattern differently under varying conditions. The measured κ remained close to zero for y-polarization but became significantly nonzero for x-polarization, demonstrating that looped trajectories contribute to interference fringes when near-field effects are enhanced through material-induced enhancement.

While the κ was enhanced by utilizing near-field components of the photon wave function and material-induced effects in[78], a non-zero κ, purely attributed to length scale-dependent boundary condition effects on the superposition principle, was observed in a completely different wavelength domain in[79]. The experiment was designed to control the effects of non-classical paths, allowing the researchers to increase or decrease the effect by adding or removing obstructions, providing definitive proof of their existence. A precision triple-slot setup as shown in Fig. 7 in the centimeter-wave domain was employed, using pyramidal horn antennas and specially designed composite materials as microwave absorbers. To minimize electromagnetic noise and interference, the experiment was conducted in a remote location, effectively simulating an anechoic chamber. Since etching slits in an absorbing layer at this scale was impractical, the experiment used absorbing slots surrounded by free space to approximate infinitely large boundaries. The modified expression for κ is defined based on the magnitude of the Poynting vector at specific detector positions and is calculated by measuring power values for different slot combinations,

$$\kappa' = \frac{P_0 - (P_{ABC} - P_{AB} - P_{BC} - P_{AC} + P_A + P_B + P_C)}{max(P_0)} \tag{34}$$

A pyramidal horn antenna, operating at a 5 cm wavelength, emitted electromagnetic waves directed at 10 cm-wide slots with a 13 cm inter-slot distance. The slots were constructed from composite materials: two layers of Eccosorb SF6.0 (a near-perfect microwave absorber) with an aluminium layer sandwiched in between to enhance absorption, particularly of back-reflected beams. A detector horn antenna, mounted on a moving rail, collected power measurements at various positions. The source and detector were placed 2.5 meters apart (1.25 meters between the source and slot plane, and the same distance between the slot and detector plane), and the values of

κ' showed modulation as a function of detector position.To ensure that the measurement time scale was sufficient, an antenna radiation pattern was recorded before measuring each slot combination. The background patterns remained stable throughout, confirming that noise fluctuations occurred on a much longer timescale than the measurement period. Background levels were averaged before and after each measurement to minimize bias, and the order of slot combinations was randomized to eliminate systematic errors. To independently verify that the observed κ' was not due to unaccounted experimental errors, absorbers (baffles) were introduced perpendicular to the slots to gradually suppress the effects of non-classical paths. As suggested in[76], "hugging paths"–which cross the slit plane twice–are the primary contributors to κ'. By systematically increasing the baffle size, a clear decrease in κ' was observed, confirming that hugging paths dominate its non-zero value.

A key potential error in observing a non-zero κ' is detector non-linearity–if the detector response deviates from linearity with increasing power, it could introduce a false non-zero. To rule this out, a detailed analysis using spline interpolation and polynomial fitting was conducted. The non-linearity effects estimated through these models were found to be at least two to three orders of magnitude smaller than the measured κ', demonstrating that detector non-linearity could not account for the observed values. Additionally, potential non-linearity in the source was ruled out, as the source was operated at a constant power.

While the slit experiment typically results in a small third-order interference term, it was theoretically shown[80] that higher-order interference can arise within the standard second quantization framework due to nonlinear effects in multipartite interactions. An increased value of nonzero third-order interference can be observed with current technologies, such as nonlinear optics or Bose-Einstein condensates.[81] demonstrated an experiment using a 'nonlinear triple slit', which consists of three laser beams interacting in an optically nonlinear crystal. The authors showed that higher-order interference can be turned on and off by modulating the nonlinear interactions in the system. A beam with a wavelength of nanometers is used, and the parameter κ is found to be 0.0334 ± 0.0002.A study[82] has established that interference of order $(2M+1)$ and higher vanishes for M particles. Furthermore, it introduced generalized many-particle Sorkin parameters, which are predicted to be zero if Born's rule holds. Many-particle higher-order interference has been experimentally demonstrated using a five-slit setup with a coherent state at a 633 nm wavelength, where the mean photon number was varied[83]. The study demonstrated that fifth-order interference is constrained to $10^{-}3$ in the intensity-correlation regime and $10^{-}2$ in the photon-correlation regime. The search for a genuine non-zero Sorkin parameter continues, pushing the boundaries of our understanding of higher-order interference. Future experiments with advanced photon sources and detection techniques may provide deeper insights into this fundamental question.

4 Conclusion and Outlook

The exploration of interference phenomena stands as a cornerstone in our understanding of quantum mechanics. From the fundamental second-order correlation measurements $(g^{(2)})$ to the more sophisticated Hong-Ou-Mandel interference effects, these experimental observations not only validate theoretical frameworks but also challenge our classical intuitions about the nature of reality. The $g^{(2)}$ correlation function has proven invaluable for distinguishing quantum from classical light, providing a robust metric for characterizing non-classical photon statistics. Meanwhile, the HOM effect–where identical photons entering a BS through different ports demonstrate fourth-order interference by emerging together–has become emblematic of quantum behavior with no classical analog. Yet, as discussed in this article, even this quintessentially quantum phenomenon can be mimicked by classical fields through careful phase control between classical pulses, blurring the boundary between quantum and classical descriptions. This remarkable ability to reproduce ostensibly quantum effects through classical means raises profound questions about the true nature of the quantum-classical divide. Rather than viewing these domains as fundamentally separate, perhaps we should understand them as different mathematical frameworks describing the same underlying reality, with quantum mechanics offering a more general description that reduces to classical physics under appropriate conditions. The investigation of higher-order interference, initiated by Sorkin's hierarchical framework, represents the next frontier in this ongoing inquiry. Sorkin's parameter κ, designed to quantify departures from the quantum superposition principle, offers a tantalizing window into possible physics beyond standard quantum mechanics. Despite numerous experimental efforts, a conclusive measurement of a non-zero Sorkin parameter that withstands all experimental scrutiny remains elusive. The technical challenges are formidable–requiring unprecedented precision in phase stability, detector efficiency, and background suppression–yet the potential rewards are equally substantial. Should future experiments definitively establish a non-zero Sorkin parameter, the implications would be revolutionary, potentially necessitating modifications to quantum theory itself. Conversely, increasingly precise null results would further cement quantum mechanics as a complete description of interference phenomena, placing ever-tighter constraints on alternative theories. As experimental techniques continue to advance, particularly in integrated photonics, quantum dot single-photon sources, and superconducting detector technology, we stand at the threshold of resolving these fundamental questions. The story of interference in quantum mechanics thus remains unfinished–a vibrant field of inquiry where fundamental questions about the nature of reality continue to drive both theoretical innovation and experimental ingenuity. The path forward lies not merely in refining existing experiments, but in developing entirely new paradigms for probing quantum interference at ever-higher orders and with unprecedented precision. Whether these investigations ultimately reveal physics beyond standard quantum mechanics or further validate its remarkable descriptive power, they will undoubtedly deepen our understanding of the fundamental principles governing our universe.

Publisher's Note

Funding

US acknowledges partial support provided by the National Quantum Mission of the Department of Science and Technology.

Data Availability

This manuscript has no associated data, as it is a theoretical review.

Declarations

Conflict of Interest

The authors declare that there are no Conflict of interest or Conflict of interest directly or indirectly related to this work.

Received: 26 March 2025 Accepted: 11 June 2025

References

1. Feynman RP, Leighton RB, Sands M (1963 and 1965) *The Feynman Lectures on Physics, Vol. 1 and Vol. 3*. Addison-Wesley, Reading, MA. Vol. 1: Mainly Mechanics, Radiation, and Heat; Vol. 3: Quantum Mechanics
2. Sinha U, Sahoo SN, Singh A, Joarder K, Chatterjee R, Chakraborti S (2019) Single-photon sources. Opt Photon News 30(9):32–39
3. Sinha U (2023) Saumya Ranjan Behera, and Mehak Layal. Chapter one - photon sources and their applications in quantum science and technologies. 68:1–65
4. Dirac P, Polkinghorne JC (1958) The principles of quantum mechanics. Phys Today 11(6):32–33
5. Kim MS, Son W, Bužek V, Knight PL (2002) Entanglement by a beam splitter: Nonclassicality as a prerequisite for entanglement. Phys Rev A 65:032323
6. Makarov DN, Gusarevich ES, Goshev AA, Makarova KA, Kapustin SN, Kharlamova AA, Tsykareva YV (2021) Quantum entanglement and statistics of photons on a beam splitter in the form of coupled waveguides. Sci Rep 11(1):10274
7. Hanbury Brown R, Twiss RQ (1956) Correlation between photons in two coherent beams of light. Nature 177(4497):27–29
8. Ghosh R, Hong CK, Ou ZY, Mandel L (1986) Interference of two photons in parametric down conversion. Phys Rev A 34:3962–3968
9. Hong CK, Ou ZY, Mandel L (1987) Measurement of subpicosecond time intervals between two photons by interference. Phys Rev Lett 59:2044–2046
10. Ghosh R, Mandel L (1987) Observation of nonclassical effects in the interference of two photons. Phys Rev Lett 59:1903–1905
11. Ou ZY (1988) Quantum theory of fourth-order interference. Phys Rev A 37:1607–1619
12. Shih YH, Alley CO (1988) New type of einstein podolsky-rosen-bohm 26 december 1988 experiment using pairs of light quanta produced by optical parametric down conversion. Phys Rev Lett 61:2921–2924

13. Fearn H, Loudon R (1989) Theory of two-photon interference. J Opt Soc Am B 6(5):917–927
14. Rarity JG, Tapster PR (1990) Two-color photons and nonlocality in fourth-order interference. Phys Rev A 41:5139–5146
15. Sadana S, Ghosh D, Kaushik Joarder A, Lakshmi N, Sanders BC, Sinha U (2019) Near-100 light and the role of complementarity. Phys Rev A 100:013839
16. Jin R-B, Shimizu R (2018) Extended wiener–khinchin theorem for quantum spectral analysis. Optica 5(2):93–98
17. Grice WP, Walmsley IA (1997) Spectral information and distinguishability in type-ii down-conversion with a broadband pump. Phys Rev A 56:1627–1634
18. Ou ZY (2006) Temporal distinguishability of an n-photon state and its characterization by quantum interference. Phys Rev A 74:063808
19. Tichy MC, Lim H-T, Ra Y-S, Mintert F, Kim Y-H, Buchleitner A (2011) Four-photon indistinguishability transition. Phys Rev A 83:062111
20. Ra Y-S, Tichy MC, Lim H-T, Kwon O, Mintert F, Buchleitner A, Kim Y-H (2013) Observation of detection-dependent multi-photon coherence times. Nat Commun 4:2451
21. Ra Y-S, Tichy MC, Lim H-T, Kwon O, Mintert F, Buchleitner A, Kim Y-H (2013) Nonmonotonic quantum-to-classical transition in multiparticle interference. Proc Natl Acad Sci 110(4):1227–1231
22. Tichy MC (2014) Interference of identical particles from entanglement to boson-sampling. J Phys B: Atom Mol Opt Phys 47(10):103001
23. Li B, Yuan B, Chen C, Xiang X, Quan R, Dong R, Zhang S, Jin R-B (2023) Spectrally resolved two-photon interference in a modified hong–ou–mandel interferometer. Opt Laser Technol 159:109039
24. Ge Z, Han Z-Q-Z, Yang F, Wang X-H, Li Y-H, Li Y, Gao M-Y, Chen R-H, Niu S-J, Xie M-Y, Zhou Z-Y, Shi B-S (2024) Quantum entanglement and interference at 3 μm. Sci Adv 10(10):eadm7565
25. Mann F, Chrzanowski HM, Gewers F, Placke M, Ramelow S (2024) Hong-ou-mandel interference of two photons of vastly different color. *Quantum 2.0 Conference and Exhibition*, page QM2B.6
26. Legero T, Wilk T, Hennrich M, Rempe G, Kuhn A (2004) Quantum beat of two single photons. Phys Rev Lett 93:070503
27. Li B, Chen C, Xiang X, Quan R, Dong R, Zhang S, Hao X, Jin R-B (2023) Complete spectral characterization of biphotons by simultaneously determining their frequency sum and difference in a single quantum interferometer. Phys Rev A 108:023713
28. Duan L, Aojie X, Wang L, Zhang Y (2024) Accessing the spectrum of a single-photon by the hong-ou-mandel interference. Opt Express 32(4):5418–5428
29. Li Bai Hong, Wang Zhuo Zhuo, Li Qi Qi, Wang Peng Long, Chen Chang Hua, Yuan Bo Xin, Zhang Xiao Fei (2025) Comprehensive interference characteristics of a three-parameter hong-ou-mandel interferometer. J Opt Soc Am B 42(1):80–92
30. Edamatsu K, Shimizu R, Itoh T (2002) Measurement of the photonic de broglie wavelength of entangled photon pairs generated by spontaneous parametric down-conversion. Phys Rev Lett 89:213601
31. Thiel V, Davis A, Sun K, D'Ornellas P, Jin X-M, Smith BJ (2020) Single-photon characterization by two-photon spectral interferometry. Opt Express 28(13):19315–19324
32. Olavo Cosme S, Pádua FA, Bovino AM, Sciarrino F, De Martini F (2008) Hong-ou-mandel interferometer with one and two photon pairs. Phys Rev A 77:053822
33. Rarity JG, Tapster PR, Loudon R (2005) Non-classical interference between independent sources. J Opt B: Quant Semiclass Opt 7(7):S171
34. Fabre N, Amanti M, Baboux F, Keller A, Ducci S, Milman P (2022) The hong-ou-mandel experiment: from photon indistinguishability to continuous-variable quantum computing. Eur Phys J D 76(10):196
35. Wei Y-J, He Y-M, Chen M-C, Yi-Nan H, He Yu, Dian W, Schneider C, Kamp M, Höfling S, Chao-Yang L, Pan J-W (2014) Deterministic and robust generation of single photons from a single quantum dot with 995% indistinguishability using adiabatic rapid passage. Nano Lett 14(11):6515–6519 (**PMID: 25357153**)
36. Senellart P, Solomon G, White A (2017) High-performance semiconductor quantum-dot single-photon sources. Nat Nanotechnol 12:1026–1039
37. Ollivier H, Thomas SE, Wein SC, Maillette de Buy Wenniger I, Coste N, Loredo JC, Somaschi N, Harouri A, Lemaitre A, Sagnes I, Lanco L, Simon C, Anton C, Krebs O, Senellart P (2021) Hong-ou-mandel interference with imperfect single photon sources. Phys Rev Lett 126:063602
38. Jin R-B, Gerrits T, Fujiwara M, Wakabayashi R, Yamashita T, Miki S, Terai H, Shimizu R, Takeoka M, Sasaki M (2015) Spectrally resolved hong-ou-mandel interference between independent photon sources. Opt Express 23(22):28836–28848
39. de Riedmatten H, Marcikic I, Tittel W, Zbinden H, Gisin N (2003) Quantum interference with photon pairs created in spatially separated sources. Phys Rev A 67:022301
40. Mosley PJ, Lundeen JS, Smith BJ, Wasylczyk P, U'Ren AB, Silberhorn C, Walmsley IA (2008) Heralded generation of ultrafast single photons in pure quantum states. Phys Rev Lett 100:133601
41. Wang S, Liu C-X, Li J, Wang Q (2019) Research on the hong-ou-mandel interference with two independent sources. Sci Rep 9:2045–2322
42. Kaltenbaek R, Blauensteiner B, Żukowski M, Aspelmeyer M, Zeilinger A (2006) Experimental interference of independent photons. Phys Rev Lett 96:240502
43. Jin R-B, Zhang J, Shimizu R, Matsuda N, Mitsumori Y, Kosaka H, Edamatsu K (2011) High-visibility nonclassical interference between intrinsically pure heralded

single photons and photons from a weak coherent field. Phys Rev A 83:031805

44. Halder M, Beveratos A, Gisin N, Scarani V, Simon C, Zbinden H (2007) Entangling independent photons by time measurement. Nat Phys 3:692–695
45. Sipahigil A, Jahnke KD, Rogers LJ, Teraji T, Isoya J, Zibrov AS, Jelezko F, Lukin MD (2014) Indistinguishable photons from separated silicon-vacancy centers in diamond. Phys Rev Lett 113:113602
46. Bernien H, Childress L, Robledo L, Markham M, Twitchen D, Hanson R (2012) Two-photon quantum interference from separate nitrogen vacancy centers in diamond. Phys Rev Lett 108:043604
47. Waltrich R, Klotz M, Agafonov VN, Kubanek A (2023) Two-photon interference from silicon-vacancy centers in remote nanodiamonds. Nanophoton 12(18):3663–3669
48. Sipahigil A, Goldman ML, Togan E, Chu Y, Markham M, Twitchen DJ, Zibrov AS, Kubanek A, Lukin MD (2012) Quantum interference of single photons from remote nitrogen-vacancy centers in diamond. Phys Rev Lett 108:143601
49. Flagg EB, Muller A, Polyakov SV, Ling A, Migdall A, Solomon GS (2010) Interference of single photons from two separate semiconductor quantum dots. Phys Rev Lett 104:137401
50. Gera S, Wallace C, Flament M, Scriminich A, Namazi M, Kim Y, Sagona-Stophel S, Vallone G, Villoresi P, Figueroa E (2024) Hong-ou-mandel interference of single-photon-level pulses stored in independent room-temperature quantum memories. npj Quant Informat 10(1):10
51. Keyu S, Zhong Y, Zhang S, Li J, Zou C-L, Wang Y, Yan H, Zhu S-L (2022) Quantum interference between nonidentical single particles. Phys Rev Lett 129:093604
52. Pan J-W, Bouwmeester D, Weinfurter H, Zeilinger A (1998) Experimental entanglement swapping: Entangling photons that never interacted. Phys Rev Lett 80:3891–3894
53. Basso Basset F, Rota MB, Schimpf C, Tedeschi D, Zeuner KD, Covre da Silva SF, Reindl M, Zwiller V, Jöns KD, Rastelli A, Trotta R (2019) Entanglement swapping with photons generated on demand by a quantum dot. Phys Rev Lett 123:160501
54. Michler M, Mattle K, Weinfurter H, Zeilinger A (1996) Interferometric bell-state analysis. Phys Rev A 53:R1209–R1212
55. Żukowski M, Zeilinger A, Horne MA, Ekert AK (1993) “Event-ready-detectors” bell experiment via entanglement swapping. Phys Rev Lett 71:4287–4290
56. Bouwmeester D, Pan J-W, Mattle K, Eibl M, Weinfurter H, Zeilinger A (1997) Experimental quantum teleportation. Nature 390(6660):575–579
57. de Riedmatten H, Marcikic I, van Houwelingen J, Tittel W, Zbinden H, Gisin N (2005) Long-distance entanglement swapping with photons from separated sources. Phys Rev A 71:050302
58. Jin J, Grimau Puigibert M, Giner L, Slater JA, Lamont M, Verma VB, Shaw MD, Marsili F, Nam SW, Oblak D, Tittel W (2015) Entanglement swapping with quantum-memory-compatible photons. Phys Rev A 92:012329
59. Hofmann J, Krug M, Ortegel N, Gérard L, Weber M, Rosenfeld W, Weinfurter H (2012) Heralded entanglement between widely separated atoms. Science 337(6090):72–75
60. Pan J-W, Chen Z-B, Chao-Yang L, Weinfurter H, Zeilinger A, Żukowski M (2012) Multiphoton entanglement and interferometry. Rev Mod Phys 84:777–838
61. Azuma K, Economou SE, Elkouss D, Hilaire P, Jiang L, Lo H-K, Tzitrin I (2023) Quantum repeaters: From quantum networks to the quantum internet. Rev Mod Phys 95:045006
62. Singh S, Sharma V, Kumar V, Samanta GK (2021) Variation of the hong-ou-mandel interference dip with crystal length. *2021 Conference on Lasers and Electro-Optics Europe and European Quantum Electronics Conference*, page 26
63. Lyons A, Knee GC, Bolduc E, Roger T, Leach J, Gauger EM, Faccio D (2018) Attosecond-resolution hong-ou-mandel interferometry. Sci Adv 4(5):eaap9416
64. Branning D, Migdall AL, Sergienko AV (2000) Simultaneous measurement of group and phase delay between two photons. Phys Rev A 62:063808
65. Giovannini D, Romero J, Potocek V, Ferenczi G, Speirits F, Barnett SM, Faccio D, Padgett MJ (2015) Spatially structured photons that travel in free space slower than the speed of light. Science 347(6224):857–860
66. Lyons A, Roger T, Westerberg N, Vezzoli S, Maitland C, Leach J, Padgett MJ, Faccio D (2018) How fast is a twisted photon? Optica 5(6):682–686
67. Meskine O, Descamps E, Keller A, Lemaître A, Baboux F, Ducci S, Milman P (2024) Approaching maximal precision of hong-ou-mandel interferometry with nonperfect visibility. Phys Rev Lett 132:193603
68. Chen Y, Hong L, Chen L (2022) Quantum interferometric metrology with entangled photons. Front Phys 10:892519
69. Abouraddy AF, Nasr MB, Saleh B, Sergienko AV, Teich MC (2002) Quantum-optical coherence tomography with dispersion cancellation. Phys Rev A 65:053817
70. Nasr MB, Saleh B, Sergienko AV, Teich MC (2003) Demonstration of dispersion-canceled quantum-optical coherence tomography. Phys Rev Lett 91:083601
71. Jin R-B, Zeng Z-Q, You C, Yuan C (2024) Quantum interferometers: Principles and applications. Prog Quant Electron 96:100519
72. Sorkin RD (1994) Quantum mechanics as quantum measure theory. Mod Phys Lett A 09(33):3119–3127
73. Sinha U, Couteau C, Jennewein T, Laflamme R, Weihs G (2010) Ruling out multi-order interference in quantum mechanics. Science 329(5990):418–421
74. Söllner I, Gschösser B, Mai P, Pressl B, Vörös Z, Weihs G (2012) Testing born’s rule in quantum mechanics for three mutually exclusive events. Foundat Phys 42(6):742–751

75. Kauten T, Keil R, Kaufmann T, Pressl B, Brukner C, Weihs G (2017) Obtaining tight bounds on higher-order interferences with a 5-path interferometer. New J Phys 19(3):033017
76. Sawant R, Samuel J, Sinha A, Sinha S, Sinha U (2014) Nonclassical paths in quantum interference experiments. Phys Rev Lett 113:120406
77. Sinha A, Vijay AH, Sinha U (2015) On the superposition principle in interference experiments. Sci Rep 5(1):10304
78. Magaña-Loaiza OS, De Leon I, Mirhosseini M, Fickler R, Safari A, Mick U, McIntyre B, Banzer P, Rodenburg B, Leuchs G, Boyd RW (2016) Exotic looped trajectories of photons in three-slit interference. Nat Commun 7(1):13987
79. Rengaraj G, Prathwiraj U, Sahoo SN, Somashekhar R, Sinha U (2018) Measuring the deviation from the superposition principle in interference experiments. New J Phys 20(6):063049
80. Rozema LA, Zhuo Z, Paterek T, Dakić B (2021) Higher-order interference between multiple quantum particles interacting nonlinearly. Phys Rev A 103:052204
81. Namdar P, Jenke PK, Calafell IA, Trenti A, Radonjić M, Dakić B, Walther P, Rozema LA (2023) Experimental higher-order interference in a nonlinear triple slit. Phys Rev A 107:032211
82. Pleinert M-O, von Zanthier J, Lutz E (2020) Many-particle interference to test born's rule. Phys Rev Res 2:012051
83. Pleinert M-O, Rueda A, Lutz E, von Zanthier J (2021) Testing higher-order quantum interference with many-particle states. Phys Rev Lett 126:190401

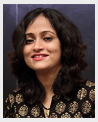

Urbasi Sinha is a Professor at the Raman Research Institute (RRI) in Bangalore, India and a Canada Excellence Research Chair at the University of Calgary, Canada and is the cofounder of a deep tech quantum start-up, QuSyn Technologies. She heads the Quantum Information and Computing lab at RRI and is an associate faculty member at both IQC and Perimeter Institute, Canada. Sinha completed her PhD and M.Sc. in Physics at Cambridge University as a Gates Cambridge and Nehru-Chevening scholar respectively. Her research focuses on quantum information processing, secure quantum communication, and precision tests of quantum mechanics using single and entangled photons. Prof. Sinha has been associated with India's National Quantum Mission (NQM) since its inception, first as a member of the core DPR committee and now as the lead PI for the Technology group working on a multi node quantum repeater network for entanglement distribution based quantum communication as a part of the Quantum Communications hub. She has also been appointed the NQM nodal point at the Open Quantum Institute in Geneva in addition to being an advisory board member for the same. Her recognitions include the Homi Bhabha Fellowship (2017), ICTP-ICO Gallieno Denardo Award (2018), and recognition among Asia's Top 100 scientists (2019). She received the Simon's Emmy Noether Fellowship at the Perimeter Institute (2020-2023) and led the winning team at the 2020 BRICS Future Skills Challenge in Quantum Technology. Recent honours include the ASSOCHAM Women in Cyber award (2021), SIES Chandrasekarendra Saraswathi National Eminence award (2023), a Distinguished International Associate award from the Royal Academy of Engineering, UK (2024), the Rashtriya Vigyan Puraskar: Yuva Shanthi Swarup Bhatnagar award from the Indian government (2024), the Gates Cambridge Impact Prize (2025) and the Lakshmipat Singhania IIM Lucknow National Eminence Award in Science and Technology (2025).

Dr. Debadrita Ghosh is currently working as a Project Scientist-C in the Quantum Information and Computing (QuIC) Lab at the Raman Research Institute, Bangalore. She completed her M.Sc. in Physics from Presidency College, Kolkata, and carried out her post-M.Sc. research in the QuIC lab. She earned her Ph.D. in Experimental Physics from the University of Göttingen, Germany, where her research focused on correcting optical aberrations in super-resolution microscopy. With over 10 years of experience in aligning optical components to construct complex experimental setups, she has developed expertise in building cuttingedge single-photon sources and applying this technology to quantum optics and related fields. Her skills also include optical imaging, microscopy, and precision instrumentation. In addition to her research role, she serves as the Director and CTO of the quantum startup QuSyn Technologies.